Thermally Activated Jamming in Ultrasonic Powder Compaction

Title: Thermally activated jamming in ultrasonic powder compaction

Authors: *Austin A. Ward*[1†], *Christopher A. Hareland*[1†], *Nathan E. Palmerio*[1], *Zachary C. Cordero**[2]

Affiliations:

1. Materials Science and NanoEngineering, Rice University, Houston, TX 77005
2. Aeronautics and Astronautics, MIT, Cambridge, MA 02139

[†]Authors contributed equally to this work

Corresponding author: Zachary Cordero; zcordero@mit.edu; 617-253-8821

Abstract: We have assessed the role of thermal softening in ultrasonic powder compaction by comparing the densification behaviors of nominally pure Cu and a thermally stable CuTa alloy. These materials have similar thermal properties, but pure Cu softens at much lower temperatures than does the CuTa alloy, thus allowing us to isolate thermal softening effects. Using a specialized ultrasonic powder compaction setup, we collected *in situ* measurements of relative density, sonotrode power consumption, and temperature, which together provided a time-dependent geometric hardening parameter that reflects the structure of the compact. The geometric hardening data for the pure Cu powder revealed three distinct stages of densification: an initial particle rearrangement stage; a jamming transition where strong junctions develop between particles; and a final stage characterized by compatible plastic deformation. By contrast, the geometric hardening data for the thermally stable CuTa powder showed that it remained a weak fluidized granular medium, despite experiencing higher normal pressures, oscillation amplitudes, and temperatures. The contrasting behaviors of the Cu and the CuTa powders suggest that a thermally activated

This is the author manuscript accepted for publication and has undergone full peer review but has not been through the copyediting, typesetting, pagination and proofreading process, which may lead to differences between this version and the Version of Record. Please cite this article as doi: 10.1002/adem.202001019.

jamming transition drives interparticle junction growth and densification in ultrasonic powder compaction.

Keywords: ultrasonic processing, powder consolidation, powder processing, nanocrystalline metals, grain growth

1. Introduction

Ultrasonic powder compaction is a promising technique for synthesizing bulk components from thermally unstable materials, such as nanostructured reactive materials[1, 2] and metallic glasses,[3] which are easy to prepare in powder form but challenging to densify. The process is a uniaxial die compaction technique in which the upper punch oscillates perpendicular to the loading axis at ultrasonic frequency. This shearing motion causes rapid consolidation as well as a brief thermal excursion as plastic work is converted into heat. The temperature rise during ultrasonic compaction aids densification;[3, 4] however, the peak temperature must be minimized to preserve the structure and properties of thermally unstable powder feedstock. Thus, there exists a set of optimal processing conditions that fully densifies a given feedstock powder while minimizing thermally activated structural evolution. Predicting such optimal parameter sets for ultrasonic compaction remains a challenge because the linkages between process variables, material properties, and densification are poorly understood.

The common approach of using classical powder metallurgy results to model the densification is complicated by the exotic conditions in ultrasonic powder compaction. A typical ultrasonic compaction cycle lasts several seconds, produces pellets with a height on the order of 1 mm, and uses a sonotrode oscillation frequency on the order of 10 kHz with an oscillation amplitude on the order of 10 μm. These parameters correspond to ~10^4 oscillation cycles, macroscopic shear strain rates of ~10^3 s^{-1}, and cumulative plastic shear strains of ~10^3. Such high strain rates and deviatoric strains are not encountered in standard compaction processes used in powder metallurgy, which

tend to be much slower and involve relatively low deviatoric stress and strain components (notable exceptions to this generalization include roll compaction[5, 6] and explosive compaction[7-9]). As a result, the underlying assumptions of conventional powder metallurgy frameworks often conflict with the behaviors expected in ultrasonic compaction. The micromechanical analysis of powder compaction due to Fleck and co-workers, for example, assumes that the particles undergo affine deformation during densification,[10-14] an assumption that is strongly violated in the early stages of ultrasonic powder compaction. There are similar problems with most of the standard treatments of metal powder compaction in the open literature.[15-18] More recent finite element simulations of junction growth under oscillatory shear loading are also limited in that they only consider small numbers of particles, relatively low strain-rates, and few oscillation cycles.[19-21]

An alternative approach for describing ultrasonic powder compaction is to consider the compact as a granular medium with frictional and cohesive particle contacts. There have been many studies on particle rearrangement and densification in granular media during oscillatory shear loading that are relevant to the early stages of ultrasonic powder compaction,[22-24] as well as many studies that link the far-field applied stresses and structure of the powder charge to the loading conditions at individual contacts.[10-14, 25-27] However, experiments and theoretical analyses of granular media typically use or assume isothermal particles with fixed amounts of cohesion and internal friction. This is clearly not the case in ultrasonic powder compaction, where the particle contacts have internal friction and cohesion parameters that change over time, the particles deform plastically, and the local temperature can strongly influence the behavior at particle contacts. Thus, standard granular mechanics frameworks also fail to capture some of the key physics in ultrasonic compaction.

Ultrasonic powder compaction involves a combination of process conditions and particle behaviors that, to our knowledge, have not been studied in detail. In the present work we address this gap in understanding by using ultrasonic powder compaction to densify pure nanocrystalline Cu powder as well as a thermally stable Cu-10Ta (at.%) alloy. We focused on these two materials because they

have similar thermal properties but very different mechanical properties; in particular, the CuTa alloy retains its strength to much higher temperatures than does the Cu powder,[28, 29] thus allowing us to isolate the effects of thermal softening on densification. We assessed the consolidation and structural evolution behaviors of these different powders using a servo-driven ultrasonic welder that can measure the height of the compact with micron-accuracy, thereby enabling accurate *in situ* measurements of the relative density. By combining these relative density measurements with *in situ* measurements of the temperature within the compact and the power consumed by the sonotrode, we gain mechanistic insights into the particle-scale phenomena that control the densification behavior of the powder charge. These results represent an important first step towards a general framework for predicting processing parameters (e.g. oscillation amplitude, normal pressure) that minimize the thermal excursion during ultrasonic powder compaction to create compacts with high relative density and non-equilibrium microstructures.

2. Materials and methods

The nanocrystalline Cu powder was prepared via high-energy ball milling of nominally pure Cu powder (sourced from Alfa Aesar) in a SPEX 8000M for 10 hours under an Ar atmosphere. The ball mill was fitted with a fan to cool the vial during milling. Milling was performed using a 10 g powder charge, a 5:1 ball-to-powder mass ratio, and 0.8 wt.% stearic acid as a process control agent. The as-milled powder was sieved to remove particles with a diameter greater than 100 μm. The resulting nanocrystalline Cu powder consisted of platelet-shaped particles (**Figure 1a**), with a mean thickness of 6 μm and a mean spherical-equivalent diameter (d) of 18 μm. The cumulative particle size distribution is shown in **Figure 1c**. High-resolution scanning electron microscopy of cross-sectioned as-milled particles revealed 6% porosity in the form of closed nanopores with a mean circular-equivalent diameter of 10 nm. Stereological measurements on these particles gave an average grain size of 70 nm.

The thermally stable CuTa alloy powder (provided by Army Research Laboratory) was prepared via high-energy cryo-milling for 8 hours under an Ar atmosphere, following the same milling procedure described in [30]. The particles were equiaxed and irregularly shaped (**Figure 1b**), with a mean spherical-equivalent diameter of 9 μm, half that of the pure Cu powder. The cumulative particle size distribution for the CuTa powder is shown in **Figure 1c** as well. Although not measured in the present work, the structure of CuTa powder with a similar composition and processing history was previously found to comprise a Cu matrix with an average grain size of 50 nm and Ta-rich precipitates that ranged in diameter from 3 to 30 nm.[29]

The ultrasonic compaction experiments were performed at room temperature using an instrumented servo-driven Tech-Sonic 3020S ultrasonic spot welder, shown schematically in **Figure 2**. The powder charge was contained within a cylindrical tool steel die with a 1 cm inner diameter. The sonotrode, which has a diameter slightly smaller than 1 cm, serves as the punch during the powder compaction process. The work surface of the sonotrode features square-pyramidal knurls with a height of 190 μm and a width of 400 μm. This welder provides *in situ* measurements of the compact height, which can be used together with the known mass of the powder charge and the inner diameter of the die to compute the instantaneous relative density. The welder also provides *in situ* measurements of the peak power required to drive the ultrasonic transducer at an oscillation frequency of 20 kHz over the prescribed oscillation amplitude. Calibration experiments without a workpiece showed that machine losses were negligible. Thus, essentially all the power consumed by the ultrasonic transducer is deposited into the powder compact as mechanical work. This allows us to directly relate the power consumption to the shear strength of the compact, as discussed in Section 4.

To measure the thermal excursion in select consolidation experiments, a fine-gauge K-type thermocouple (AWG 42; 60 μm bead diameter) was embedded inside the charge. This thermocouple had a temporal resolution on the order of 0.1 ms and was the finest gauge that could survive the experiments without breaking. A Polytec OFV-5000 laser vibrometer was used to

ensure the sonotrode oscillation amplitude was constant during the consolidation experiment. The initial mass and height of the powder charge were typically 0.5 g and 1.4 mm, corresponding to a relative density of approximately 0.5.

The Vickers hardness values of the recovered materials were measured using a Leco LM-310AT microhardness tester with loads ranging from 0.25–2.0 N and a five second hold. A TEM lamella was extracted from the center of a compact using the focused ion beam (FIB) lift-out technique in an FEI Helios NanoLab 660 DualBeam system. To minimize beam damage, the sample was thinned with a low-energy (2 kV) Ga ion beam in the final thinning step. This sample was imaged in a FEI Titan Themis operated at 300 kV.

3. Ultrasonic compaction experiments

3.1. Optimization of process parameters

In our initial set of compaction experiments, we independently varied the normal pressure (σ), oscillation amplitude (λ), and compaction time (t_c) to determine parameter sets that give strong compacts without excessive heating. The sonotrode oscillation frequency (f) was always 20 kHz. The peak compact temperature increased with oscillation amplitude and normal pressure. The nanocrystalline pure Cu powder densified in 2 to 3 seconds when the normal pressure and oscillation amplitude were greater than 20 MPa and 16 μm, respectively; lower normal pressures and oscillation amplitudes could not densify the powder, even for compaction times longer than 5 seconds. Through trial-and-error we found that the parameter ranges σ = 38–40 MPa, λ = 18–21 μm, and t_c = 2–3 s gave cohesive, dense compacts while minimizing the thermal excursion. We were unable to densify the CuTa feedstock, which remained a loose powder even under the highest normal pressure (σ = 70 MPa) and oscillation amplitude (λ = 24 μm) accessible with the current setup.

3.2. *In situ* measurements during ultrasonic compaction

Figure 3 shows representative *in situ* measurements of the compact height, relative density, temperature, and sonotrode power consumption from two compaction experiments – one using pure Cu powder with σ = 38 MPa and λ = 18 μm, and the other using the CuTa alloy with σ = 64 MPa and λ = 21 μm. These conditions represent the optimal processing parameters for Cu, and our best attempt to densify CuTa. Note that while the initial height of the CuTa compact was larger than that of the Cu compact, both compacts had similar initial relative densities. The laser Doppler vibrometry measurements confirmed that the sonotrode oscillation amplitude remained constant during these experiments.

Figure 3a shows that for the pure Cu powder, the compact height decreases rapidly during the first second of the compaction cycle then plateaus. This corresponds to an increase in relative density from 0.40 to 0.76 (**Figure 3b**). The sonotrode power (**Figure 3c**) also changes with time, transitioning from an initial period of low power consumption (0.5 kW) to a regime where the power steadily increases until reaching a final steady-state regime, where the power remains around 1.5 kW. The temperature measurements presented in **Figure 3d** show the temperature increasing over the course of the experiment to a maximum temperature of 620 K, with temperature spikes during the middle portion of the compaction cycle. Since these temperature spikes are not accompanied by spikes in the power curve, they likely correspond to localized heating events in which the fine-gauge thermocouple is in contact with powder particles undergoing shear at their contact.

To confirm that the thermal mass of the thermocouple bead does not influence the magnitude of these temperature spikes, we compare its volume (10^{-13} m^3) with the volume of material heated during the temperature spike, estimated as $\frac{4}{3}\pi L^3$, where L is the thermal diffusion distance given by $\sqrt{\alpha t_s}$. Here α is the thermal diffusivity of the powder (~10^{-4} m^2/s) and t_s is the duration of the temperature spike (~0.1 s). These values give a heated volume of 10^{-7} m^3, six orders of magnitude

larger than the volume of the thermocouple, demonstrating that the thermocouple mass should have a negligible effect on the magnitude of the temperature spike.

The CuTa powder did not form a strong compact under the processing conditions shown in **Figure 3**, despite using a higher oscillation amplitude and normal pressure than those applied to the Cu powder. The disparate consolidation behaviors of pure Cu and the CuTa alloy are reflected in the *in situ* measurements of relative density and power consumption. **Figure 3b** shows that the relative density of the CuTa compact only increased from 0.47 to 0.59 during the consolidation experiment, which is significantly less than the increase seen in the pure Cu material. The final sonotrode power consumption for the CuTa powder was also appreciably lower than that for pure Cu, despite the CuTa powder being roughly three times harder than the Cu powder. This result reflects how the CuTa powder remained a weak granular medium while the pure Cu powder transformed into a stronger porous solid.

In **Figure 3d** the *in situ* temperature measurements for the CuTa alloy are similar in form to those for the Cu powder, although the maximum temperature in the CuTa compact is ~150 K higher. Since the sonotrode power consumption is lower in the CuTa experiment than in the Cu experiment, this temperature difference likely results from residual porosity due to the lack of densification, which lowers the effective thermal conductivity of the CuTa compact. Interestingly, the CuTa temperature measurements also feature temperature spikes which are similar in magnitude to those found in the Cu data. The temperature spikes are evident in the CuTa data well after they have disappeared from the Cu data, providing additional evidence that the temperature spikes result from the motion of loose particles within the compact. Our inability to densify the CuTa powder shows that localized heating by itself does not guarantee consolidation.

3.3. Structure of compacts

The hardness of the CuTa powder recovered from the ultrasonic compaction experiments was 4.1 GPa, the same as that of the as-milled powder, indicating that the microstructure of this material was unaffected by ultrasonic processing. Since the peak temperature recorded during ultrasonic compaction of CuTa was ~760 K, which is below the temperature where this material starts to coarsen, ~875 K,[31] the lack of coarsening and attendant softening is reasonable.

Figure 4a shows an optical micrograph of a cross-sectioned Cu compact densified using σ = 40 MPa, λ = 18 μm, and t_c = 2.2 seconds. The center of the compact appears fully dense, while the left edge contains residual macroporosity, indicating that there was non-uniform plastic deformation and densification within the compact. **Figure 4b** is a bright-field TEM micrograph taken from the center of this specimen. This image shows the nanoscale grain structure of the compact, which, according to stereological measurements, had a mean circular-equivalent diameter of 120 nm, approximately twice that of the as-milled powder. The compact had a Vickers microhardness of 1.4 GPa; according to Hall-Petch data for pure copper,[32] this hardness corresponds to a grain size of 90 nm which is in rough agreement with the grain size measurement. These results show that while there is grain growth during ultrasonic powder compaction, it is possible to preserve a fine grain structure.

The porosity of the Cu compact shown in **Figure 4a** was 24% according to the Archimedes method. However, stereological measurements on the optical micrograph revealed only 2% residual macroporosity. The remaining porosity was present as closed spherical nanopores which can be seen clearly in **Figure 4b** and which ranged in size from 20 to 200 nm. The nanopores in the compact are an order of magnitude larger than the pores found in the as-milled powder. In light of recent reports of solid-state foaming in ball-milled powders,[33-35] we suspect that the pores in the as-milled Cu powder may have grown during ultrasonic compaction due to thermal expansion of trapped gases, which either were entrained in the powder during the milling process[33, 34] or were formed via the decomposition of the stearic acid process control agent.[35] We believe that further

optimization of the powder synthesis process to mitigate gas entrainment and avoid process control agents could eliminate the nanoporosity seen in **Figure 4b** to yield fully dense compacts.

In previous work examining grain growth during ultrasonic spot welding of nanocrystalline foils,[36] we demonstrated that the extent of grain growth inside the weld nugget can be related to the thermal excursion by combining *in situ* temperature measurements with a classical grain growth law. This grain growth calculation was accurate even for a nanocrystalline Ag-W alloy designed to suppress grain growth,[36] suggesting that plastic deformation during ultrasonic processing can mitigate effects that normally suppress grain growth, such as solute drag and Zener pinning. Following this same approach, we estimate the instantaneous grain size, D, within the compact during ultrasonic powder compaction by combining *in situ* temperature measurements with a grain growth equation[37] and integrating over the compaction cycle as follows:

$$D^n = D_0^n + M_0 \int_0^t \frac{1}{T(t)} \exp\left[\frac{-Q}{k_B T(t)}\right] dt. \qquad (1)$$

Here, D_0 is the initial grain size, n is the grain growth exponent, M_0 is the grain boundary mobility pre-factor, Q is an activation energy, and k_B is the Boltzmann constant. We set n = 4 and Q = 1 eV, consistent with values reported by Lu et al. in their study on grain growth in nanocrystalline Cu.[38] Using these values for n and Q and fitting the grain growth equation to the experimental data provided by Lu et al., we determined $M_0 = 3.5 \times 10^{-18}$ $m^4 \cdot K/s$. Note that Eq 1 does not account for strain-induced grain growth, an effect sometimes observed in nanocrystalline materials.[39-42]

Figure 5a shows *in situ* temperature measurements during a Cu compaction experiment using the same parameters as used in **Figure 4**. This temperature profile does not feature the temperature spikes seen in **Figure 3d**, most likely because they are stochastic, localized events and none happened close to the thermocouple in this experiment. These temperature measurements were used with Equation 1 to compute the grain size as a function of time, and the results are shown in **Figure 5b**. There is negligible grain growth during the first 1.2 seconds of the compaction experiment, followed by rapid grain growth over the remaining 1 second. The predicted final grain size is 140

nm, which is in good agreement with the experimental value (120 nm). The small discrepancy between the predicted and the experimental values may be due to pore drag from the nanopores, which tends to inhibit grain growth and preserve fine grain structures.[43, 44]

4. Structural evolution of the compact

The power consumed by the sonotrode is dissipated mainly as plastic work within the compact. Because the sonotrode oscillation amplitude is nominally constant, the increase in sonotrode power consumption seen in **Figure 3c** reflects an increase in the shear strength of the compact. Although thermal softening and grain growth lead to material softening, formation of interparticle junctions results in a net increase in shear strength as the compact transitions from a granular medium to a porous solid. We quantify this structural evolution using the geometric hardening parameter (η), defined as the ratio of the instantaneous shear strength of the compact to that of the fully dense base material. η is expected to be low for a fluidized granular medium and to approach unity when the material achieves full density. Assuming that the plastic strain is uniform and that the power consumed by the sonotrode is dissipated entirely through plastic shearing of the compact,[45] it follows that η is related to the sonotrode power consumption (P) by

$$\eta = \left(\frac{1}{\tau_{ys}}\right)\frac{P}{4\sqrt{2}\lambda f \pi r^2}, \quad (2)$$

where τ_{ys} is the shear strength of the fully dense base material and r is the radius of the die. We estimate τ_{ys} for Cu using the Khan-Huang-Liang (KHL) model for the high-rate flow stress of nanocrystalline materials.[46-48] Because nanocrystalline materials do not work-harden appreciably,[49, 50] we use a modified form of the KHL model that omits the work-hardening terms as follows:

$$\tau_{ys} = \frac{1}{\sqrt{3}}\left(a + \frac{k}{\sqrt{D}}\right)\left(\frac{\dot{\gamma}}{\dot{\gamma}^*}\right)^c \left(\frac{T_m - T}{T_m - T_0}\right)^m. \quad (3)$$

Here $\dot{\gamma}$ is the shear strain rate, given by

$$\dot{\gamma} = \frac{4\lambda f}{h}, \quad (4)$$

where h is the height of the compact. In Eq 3, $\dot{\gamma}^*$ is a reference shear strain rate of 1 s^{-1}, a and k are Hall-Petch parameters, T_m is the melting temperature, T_0 is a reference temperature, c is the strain-rate sensitivity exponent, m is the temperature sensitivity exponent, and D is the instantaneous grain size, determined using Eq 1. For pure copper, a = 40 MPa, k = 110 MPa·$\mu m^{-1/2}$, c = 0.022, and m = 1.5.[32, 51] To estimate τ_{ys} for CuTa, we use the following constitutive law taken from a study on high-rate deformation of fully dense, nanocrystalline CuTa:[52]

$$\tau_{ys} = A\left(1 + B\ln(\dot{\gamma})\right)\left(\frac{T_m - T}{T_m - T_0}\right)^C, \quad (5)$$

where A = 1 GPa, B = 0.008, and C = 1.12. For the ultrasonic compaction experiments shown in **Figure 3**, Equation 3 predicts that the shear strength $\tau_{ys}$of the nanocrystalline Cu material decreases from 320 to 180 MPa over the course of the experiment due to thermal softening and grain growth, while Equation 5 predicts that τ_{ys} of the CuTa alloy decreases from 1 GPa to 580 MPa due to thermal softening alone.

The geometric hardening data from the experiments shown in **Figure 3** are plotted against relative density in **Figure 6**. Considering that the nanocrystalline Cu powder densifies into a cohesive compact, its η values towards the end of the experiment are surprisingly low. A potential explanation for this low geometric hardening parameter is that as the knurls indent into the Cu surface, there is strain localization and intense heating near the top of the compact, giving rise to excessive thermal softening and an artificially low η.

Nevertheless, the Cu data clearly reveals three distinct stages of densification, as indicated in **Figure 6**. The first stage, spanning the relative density range 0.4–0.58, lasted ~0.3 seconds and was characterized by a low geometric hardening parameter that remained nearly constant as the powder aggregate densified. Samples recovered from this stage of the consolidation experiment were still loose powder. Considering the lack of geometric hardening and the granular nature of the compact,

we conclude that in this first stage, the powder aggregate is a fluidized granular medium, densifying via particle rearrangement under excitation by ultrasonic vibrations. This conclusion is consistent with experiments[22, 53-56] and discrete element simulations[57, 58] which show that loose granular media subjected to oscillatory loading initially densify via particle rearrangement.

In the next stage, which lasted ~1.2 seconds and spanned the relative density range 0.58–0.75, the geometric hardening parameter η increased by a factor of five, from 0.01 to 0.05. Specimens recovered from the end of this second stage were porous solids, suggesting the dramatic increase in η corresponds with a jamming transition, in which junctions grow between the particles to form a stiff, percolating network of metallurgical bonds. Because the individual Cu particles were nanoporous, with a relative density that decreased from 0.96 to ~0.80 over the course of the consolidation experiment, the packing fraction at which jamming sets on in **Figure 6** is in the range 0.62–0.78. It is interesting to note that the form of the geometric hardening curve for the Cu powder near the jamming transition closely resembles the strengthening behavior observed in previous work on jamming of a fluidized granular medium,[59-61] which revealed a 4x increment in strength as the powder charge jammed.

In the final stage of densification, densification slowed while the geometric hardening parameter η reached a maximum value of 0.065 before starting to decrease. Since the sonotrode power consumption remained nominally constant in this stage while the temperature continued to increase, this drop in η reflects softening of the base metal. Although densification slowed in this final stage, qualitative bend tests showed that the strength of the compacts continued to increase with time, demonstrating that ultrasonic shearing strengthened the interparticle bonds, presumably by disrupting oxide overlayers that encapsulated the particles.

In contrast with the behavior of the Cu powder, the geometric hardening data of the CuTa alloy reveal just a single stage of densification, in which η increased from 10^{-3} to a final value of 0.01, then hovered around this value for the remainder of the experiment. Notably, η = 0.01 is identical to

the geometric hardening parameter of the Cu powder at the onset of its jamming transition, showing how the CuTa feedstock rearranged into a dense packing, similar to the Cu material, but did not develop strong interparticle junctions, consistent with the fact that the recovered material was a loose powder.

Jamming transitions have been studied extensively using simulations of particle aggregates, which have revealed that jamming can occur under a wide range of conditions, including isostatic compaction of frictionless particles,[62] unidirectional shear of frictional particles,[63] and oscillatory shear of both frictional particles[64] and frictionless particles.[56] However, to our knowledge, the jamming transition seen in the Cu data is the first direct experimental evidence of jamming in a soft, temperature-sensitive material under oscillatory shear loading. While oscillatory shear jamming does not occur at a unique packing fraction in a polydisperse granular medium,[56] the random close-packed configuration provides a good lower-bound estimate for the packing fraction at the onset of jamming. According to the analysis by Brouwers,[65] the packing fraction F of a random close-packed aggregate of rigid platelets with a log-normal particle size distribution is given by

$$F = 1 - \chi e^{-\sqrt{2\pi}\beta(1-\chi)\varphi}, \quad (6)$$

where the fitting parameters χ and β are 0.503 and 0.374, respectively, and φ is the standard deviation of the log-normal particle size distribution. Using the experimentally determined φ of 1.2 for the as-milled Cu powder, Eq 6 predicts $F = 0.71$, which is directly in the middle of the range of the experimentally determined jamming onset. Jamming may have occurred at a higher packing fraction in our experiments than that predicted by the Brouwers model because ultrasonic vibrations can drive the Cu powder into a more organized, denser packing than a statistically random packing.[66]

5. Mechanisms of junction growth, jamming, and densification

5.1 Thermal softening at particle contacts

To summarize the experimental results, the geometric hardening data of the Cu feedstock reveal three distinct stages of ultrasonic compaction: (1) an initial particle rearrangement stage, during which the powder charge densifies but its overall strength remains low; (2) a jamming transition where the compact develops a percolating network of strong contacts; and (3) a final stage characterized by compatible plastic deformation. Comparing the geometric hardening data of the Cu and the CuTa powders demonstrates that a critical step in this sequence is junction growth during the jamming transition (Stage 2); without junction growth, the feedstock remains a fluidized granular medium, as in the case of CuTa powder. In ultrasonic spot welding and ultrasonic additive manufacturing, junction growth results from thermal softening of surface asperities due to frictional heating.[67] Similarly, the distinct consolidation behaviors of the temperature-sensitive pure Cu material and the thermally stable CuTa alloy indicate that thermal softening controls junction growth during ultrasonic powder compaction.

Several other recent studies have also hinted at the important role of temperature effects during ultrasonic compaction. Two-dimensional finite element simulations on the ultrasonic compaction of a stack of wires revealed uniform heating within the charge, as well as thermal softening and resulting densification.[4] In separate work on ultrasonic compaction of Ti-base metallic glass powder by Chen et al.[3] and aluminum powder by Liu et al.,[68] interparticle junction growth was attributed to thermal softening from transient flash heating events at particle contacts, as one particle is sheared past another. These authors used a simple frictional heating model to estimate flash heating temperature increments in the range 200–400 K for Ti powder and ~100 K for pure aluminum, which they argued was sufficient to enable the growth of strong interparticle junctions.

The temperature spikes in **Figure 3d** are on the order of 100 K, similar in magnitude to the values predicted by Liu et al. Additionally, in the case of the Cu powder, the temperature spikes coincide with the jamming transition, supporting the view that thermal softening via local temperature spikes promotes interparticle junction growth and the resulting jamming transition. However, while thermal softening clearly plays an important role in ultrasonic powder compaction, there are several

problems with the flash heating mechanism proposed by Chen et al. First, the expression that these authors used to estimate the flash heating temperature does not describe flash heating at contacting asperities, but instead gives the steady-state temperature increment at the interface between a stationary semi-infinite body and a flat pin moving with constant velocity.[69, 70] Second, Chen et al. predicted such high flash heating temperatures in part because they assumed unreasonably high interparticle contact stresses, on the order of 10 GPa,[3, 68] which titanium particles could not physically support. Third, the timescale of the temperature spikes in **Figure 3** is on the order of 0.1 s, many orders of magnitude longer than the expected lifetime of a sheared contact, which we estimate below.

In light of these discrepancies, we revisit the expected temperature increment from flash heating during ultrasonic compaction. Flash heating at particle contacts in a granular medium has been modeled extensively in the geomechanics literature because of its important role in fault weakening and shear localization during earthquakes.[71, 72] Conveniently, the particles sizes (1–100 μm), slip rates (1–10 m/s), hydrostatic pressures (10–100 MPa), and thicknesses (~1 mm) of the shear localization zones that develop in a fault during an earthquake match the conditions in ultrasonic compaction, thus enabling straightforward application of these geomechanics flash heating models to ultrasonic compaction. Following the analysis of flash heating in a granulated fault core due to Rice,[72] we estimate the flash heating temperature (T_f) at a circular interparticle contact with diameter l and shear strength τ_c using

$$T_f = T_b + \frac{\tau_c}{\rho C_p}\left(\frac{Vl}{\pi\alpha}\right)^{1/2}, \quad (7)$$

where T_b is the average temperature in the bulk of the compact, V is the tangential relative velocity of the contacting particles, and ρC_p is the volumetric heat capacity of the base material. The volumetric heat capacity ρC_p of Cu is 3.85 J/cm^3·K.[73] This same value is used to estimate ρC_p of CuTa. The thermal diffusivity of nanocrystalline Cu is 75 mm^2/s,[74] and that of the CuTa alloy is 65 mm^2/s.[75]

We estimate V using results from discrete element simulations of granular media undergoing plane shear, which have shown that particle motion correlates with the ratio of inertial forces to confining forces,[76-78] represented by the dimensionless inertial number $I = \dot{\gamma}\left(\frac{m}{\sigma d}\right)^{1/2}$, where m is the mass of a particle and d is the mean particle size. Despite the high slip rates in ultrasonic powder compaction, I is quite small (~10^{-4}). Based on the results in [76], this indicates that the compact is in the quasi-static regime characterized by intermittent particle motion, with some particles remaining stationary and others moving at velocities approaching the net slip rate. In the case of ultrasonic powder compaction, the net slip rate corresponds to the sonotrode velocity, so we set V to the root-mean-square sonotrode velocity of ~1.6 m/s.

To estimate the mean contact size l, we use the approximation formula due to Helle et al. which gives l in terms of the initial relative density of the compact $\tilde{\rho}_0$, its instantaneous relative density $\tilde{\rho}$, and the particle diameter d:[79]

$$l = \frac{d}{\sqrt{3}}\left(\frac{\tilde{\rho}-\tilde{\rho}_0}{1-\tilde{\rho}_0}\right)^{1/2}. \quad (8)$$

Although Eq 8 was originally developed to describe isostatic compaction of an aggregate of monodisperse, spherical particles, it provides a reasonable first-order estimate of the contact size in ultrasonic compaction. For the Cu powder, using $\tilde{\rho}_0$ = 0.4 and setting $\tilde{\rho}$ equal to the packing fraction at the onset of the jamming transition, 0.71, Equation 8 predicts l = 7 μm.

At a frictional interparticle contact, the shear strength of the contact τ_c is related to the normal stress of the contact σ_c by $\tau_c = \mu\sigma_c$, where μ is the friction coefficient of the contact. Here we assume μ equals the macroscopic friction coefficient of a sliding Cu/Cu contact in air, 0.4.[80] σ_c is bounded by the onset of plastic yielding; by approximating the particle contact as two indenting spheres, it can be shown that $\sigma_c \approx 6\tau_{ys}$.[79] Combining these expressions gives $\tau_c = 6\mu\tau_{ys}$.

Finally, evaluating Eq 7 with the parameters listed above gives flash heating temperature increments $\Delta T = T_f - T_b$ of 20 K for the Cu powder and 30 K for the CuTa powder. These values

are much smaller than the temperature spikes in **Figure 3d**, and likely not large enough to result in appreciable thermal softening, as previously claimed by Chen et al. The underlying reasons for the low flash heating temperatures during ultrasonic compaction of Cu alloys are (i) that the particles are relatively weak, thus limiting the maximum shear stress τ_c, and (ii) that the thermal diffusivity of Cu is high, enabling heat to rapidly diffuse from the contact into the particle core. In fact, the timescale of heat diffusion across a Cu particle, d^2/α, and the lifetime of a sheared contact, l/V, are both on the order of 1 μs, meaning the contact can thermalize as it is being sheared.

Since flash heating at isolated particle contacts cannot account for the temperature spikes in **Figure 3d** or the thermal softening required for junction growth, we consider other forms of particle motion which might reproduce the heating that drives junction growth, jamming, and densification. It is well-established that in the quasi-static regime (i.e., $I < 10^{-3}$), dense granular media exhibit shear localization along slip planes under plane-shear loading [76]. Hence, one possibility is that during ultrasonic compaction, there is shear localization within the compact, and the mating surfaces of the slip plane accommodate the sonotrode motion by rubbing against each other, resulting in frictional heating. Shearing at the slip plane would continue until the local temperature activates interparticle junction growth and seizure. Subsequently, shear localization would commence in a different, weaker region of the compact, and the process would repeat until the compact formed a percolating network of strong contacts.

We can estimate the temperature increment ΔT at a slip plane active for time t using[36]

$$\Delta T = \mu f \sigma \lambda \sqrt{\frac{\pi t}{2(\tilde{\rho}\rho C_p)(\tilde{\rho}\alpha)}}. \quad (9)$$

The thermal conductivity and the volumetric heat capacity are both scaled by the relative density to account for porosity in the compact. Assuming t is the lifetime of a temperature spike, 0.1 s, and using the material properties of Cu and the processing conditions σ = 38 MPa, λ = 18 μm, f = 20

kHz, Eq 9 predicts ΔT = 100 K for the Cu powder, in excellent agreement with the magnitude of the temperature spikes in **Figure 3c**.

Another possible frictional heating mechanism is that at the early stages of the jamming transition, the particles lock into a metastable configuration that accommodates the sonotrode oscillations via microslip at particle contacts, without gross particle motion. This physical picture is consistent with the small shear strain regime found in simulations of oscillatory shear jamming by Sastry et al.[56] Based on observations of jamming in experiments[81-83] and in discrete element method simulations,[84-86] we expect that under these conditions, a minority of the particles carry a majority of the load, with most particles behaving as spectators in the deformation process. Consequently, frictional heating via oscillatory microslip would be a rare event within the compact, with local hot spots shifting among different active contacts throughout the compact as it densifies, potentially giving rise to the sporadic temperature spikes shown in **Figure 3d**. Again, we can use Equation 9 to estimate the temperature rise at these contacts. At an active contact, we anticipate that the oscillation amplitude λ would be a fraction of the sonotrode oscillation amplitude but that the interparticle contact stress would remain near the yield condition $\sigma_c \approx 6\tau_{ys}$, resulting in significantly higher local stresses than the nominal pressure applied by the sonotrode. In Eq 9, the smaller oscillation amplitude and higher contact pressure would cancel out, resulting in a temperature increment similar to that expected for the macroscopic shear localization mechanism. Ultimately, because shear localization and interparticle microslip are expected to cause similar temperature increments, resolving whether frictional heating at the jamming transition results from shear localization, microslip at particle contacts, or some combination thereof will require *in situ* imaging to assess the kinematics of particle motion. Regardless, it is clear that thermal softening due to particle rubbing activates junction growth and the resulting jamming transition in ultrasonic powder compaction.

Finally, we consider how much thermal softening is required to drive junction growth in ultrasonic powder compaction using the ratio of the mean normal interparticle contact stress, $\bar{\sigma}_c$, to the hardness of the base material, $H \approx 6\tau_{ys}$. This ratio $\bar{\sigma}_c/H$ is analogous to the ratio of normal pressure to hardness used in the classical Tabor relation to estimate the fractional contact area between rough surfaces.[87] Under a purely isostatic stress, the compact should only densify via plastic deformation when the ratio $\bar{\sigma}_c/H$ is greater than unity; however, in ultrasonic compaction, junction growth and densification can occur at lower values of $\bar{\sigma}_c/H$ because of the multiaxial stress state. Here we estimate $\bar{\sigma}_c$ as the normal stress σ normalized by the relative density of the compact (i.e., $\sigma/\tilde{\rho}$). For the nanocrystalline Cu powder, $\bar{\sigma}_c/H$ was 0.04 at the peak of the temperature spike labeled in **Figure 3d**, which corresponded to the onset of the jamming transition. In the CuTa alloy powder, $\bar{\sigma}_c/H$ was 0.02 at the temperature spike near the end of the test in **Figure 3d**. These two values serve as rough upper and lower bounds, respectively, on the minimum ratio of $\bar{\sigma}_c/H$ required to trigger junction growth in ultrasonic compaction. Of course, higher values of this ratio should also drive junction growth and densification. This appears to have been the case in the work on ultrasonic compaction of Al powders by Liu et al.,[68] where we estimate $\bar{\sigma}_c/H$ was 0.1 at the onset of junction growth.

5.2 Other potential mechanisms: acoustic softening and associated flow

An effect sometimes used to explain junction growth in ultrasonic spot welding is acoustic softening,[88-92] which refers to a decrease in flow stress under ultrasonic excitation. Acoustic softening was first observed in uniaxial tension tests on fully dense metals, where it was found that the extent of softening scaled with the sonotrode oscillation amplitude.[93] It has since been observed during compression testing[94] and metal-forming operations,[95] and in a wide range of different materials, including pure metals[96, 97] and engineering alloys[92, 98, 99]. Acoustic softening is reversible, and the flow stress quickly recovers when the ultrasonic excitation stops.[93] Acoustic softening has important practical implications for ultrasonic powder compaction because if acoustic

softening does not require elevated temperatures, it might enable the athermal growth of interparticle junctions.

While acoustic softening is now an established phenomenon, its underlying physical mechanisms are still debated. Proposed mechanisms of acoustic softening include: thermal softening due to frictional heating between the ultrasonic transducer and the test specimen;[95] dislocation-based effects related to dislocation annihilation[104-107] and to unlocking of pinned dislocations;[93, 101-103] and stress superposition,[95, 100] which holds that the peak stress in each oscillation cycle still equals the conventional flow stress even though the mean stress appears lower. The thermal softening hypothesis conflicts with *in situ* temperature measurements that reveal a lack of heating[108] and with the nearly instantaneous recovery of strength when the ultrasonic excitation stops. Dislocation-based explanations of acoustic softening are similarly inconsistent with the reversible nature of acoustic softening. In addition, the dislocation annihilation theory of acoustic softening directly conflicts with the present results. This theory holds that the extent of softening scales with stacking fault energy.[105] Accordingly, because the stacking fault energy of the CuTa alloy is higher than that of pure Cu, this theory predicts that CuTa should soften to a greater extent than Cu and should therefore be easier to densify than pure Cu.[109] This behavior is of course the exact opposite of that observed experimentally.

In light of these issues, we contend that stress superposition is the most likely explanation of acoustic softening, but that the conventional assumption that the static stress component must be co-linear with the oscillatory stress is overly simplistic. Instead, we argue that when ultrasonic vibrations excite a fully dense metallic specimen during a uniaxial tension or compression test, the resulting multiaxial stress state oscillates between two points displaced from the uniaxial loading condition on the yield surface. As result, the material yields, but at a seemingly lower uniaxial stress. The plastic strain increment averaged over the oscillation cycle is still parallel with the uniaxial loading direction because of plastic strain normality and the biasing action of the uniaxial

load. Thus, while it appears that the flow stress is reduced when ultrasonic vibrations excite the specimen, the applied stress is in fact just probing a different region of the yield surface.

In contrast with fully dense metals, granular materials do not exhibit normality; instead they are best described by non-associated flow rules which capture effects like pressure-dependent yield, not fully matched by inelastic dilatancy.[110-112] Hence, if acoustic softening results from associated flow, as we suspect, then acoustic softening by itself cannot drive junction growth and the resulting jamming transition during ultrasonic compaction. Only after the compact has transformed into a porous solid, which can be described with an associated flow rule, would acoustic softening aid densification.

6. Conclusions

Instrumented ultrasonic compaction experiments have been used to assess the densification behaviors of a temperature-sensitive, nanocrystalline pure Cu powder and of a thermally stable CuTa alloy. While the Cu powder transformed from a weak granular medium into a strong porous solid via a jamming transition, the CuTa powder densified via particle rearrangement but resisted jamming and thus remained a loose powder. Because the main difference between the Cu and the CuTa materials is that the CuTa alloy resists thermal softening to much higher temperatures, we conclude that thermal softening drives interparticle junction growth and the resulting jamming transition in ultrasonic powder compaction.

In situ temperature measurements from a thermocouple embedded in the compact revealed intermittent temperature spikes during ultrasonic compaction of both materials. The temperature spikes coincided with the jamming transition in the Cu powder, suggesting they may facilitate junction growth. The temperature spikes had a magnitude of ~100 K and a lifetime on the order 0.1

s. While previous investigators have attributed such temperature spikes to transient flash heating at particle contacts, as one particle is sheared past another, a simple flash heating model shows that this cannot be the case, as flash heating events are too brief (~1 μs) and result in too small of a temperature increment. Instead, the temperature spikes likely arise from oscillatory slip along shear bands, which are commonly observed in granular media under plane-shear loading, and from oscillatory microslip at particle contacts, which was observed in recent simulations of oscillatory shear jamming.

We speculate that the acoustic softening effect observed during mechanical testing and deformation processing of fully dense metals is likely a manifestation of associated flow. Following this argument, because powder aggregates exhibit non-associated flow, acoustic softening cannot contribute to densification in ultrasonic powder compaction until after the jamming transition, when the compact has transformed into a porous solid.

The present conclusions align closely with our recent work on ultrasonic additive manufacturing of foils,[67, 113] which showed that thermal softening drives junction growth and welding. That work also established how the different temperature and pressure dependences of junction growth and grain growth give rise to a range of processing conditions that impart strong interlayer bonding while minimizing coarsening. This processing window can be expanded by incorporating soft, low melting point interlayer materials that facilitate junction growth at lower temperatures and pressures. Considering the clear evidence of thermally activated jamming and densification in ultrasonic powder compaction, many of the guidelines that we developed for ultrasonic additive manufacturing likely also apply to ultrasonic powder compaction. Namely, higher pressures and shorter compaction times should help mitigate coarsening. Additionally, developing mixtures of temperature-sensitive powders and thermally stable powders should expand the range of processing conditions that give strong compacts with retained nanostructures.

Acknowledgements: Funding for this work was provided by Schlumberger and by the Army Research Office through Award No. W911NF-17-1-0342. The authors thank Dr. Vikrant Palan of Polytec Inc. for loaning us the laser Doppler vibrometer; Jackson Mang, Mark Cantu, Matthew Weatherman, and Nathaniel Ocañas, all of Rice University, for assistance in performing the ultrasonic compaction experiments; and Dr. Sadegh Yazdi of CU Boulder for collecting the TEM images.

Conflict of interest: The authors declare no conflict of interest.

References

[1] S. G. Hashemabad, T. Ando, Combust. Flame **2015**, 162, 1144.

[2] S. K. Pillai, A. Hadjiafxenti, C. C. Doumanidis, T. Ando, C. Rebholz, Int. J. Appl. Ceram. Technol. **2012**, 9, 206.

[3] P. Chen, W. Liao, L. Liu, F. Luo, X. Wu, P. Li, C. Yang, M. Yan, Y. Liu, L. Zhang, Sci. Rep. **2018**, 8, 1.

[4] S. Bhavsar, S. James, Add. Manufac. **2018**, 21, 705.

[5] S. Shima, M. Yamada, Powder Metall. **1984**, 27, 39.

[6] V. Tracey, Powder Metall. **1969**, 12, 598.

[7] S. Ando, Y. Mine, K. Takashima, S. Itoh, H. Tonda, J. Mater. Process. Technol. **1999**, 85, 142.

[8] R. Prümmer, Mater. Sci. Eng. **1988**, 98, 461.

[9] R. Prümmer, Materialwiss. Werkstofftech. **1989**, 20, 410.

[10] N. A. Fleck, L. T. Kuhn, R. McMeeking, J. Mech. Phys. Solids **1992**, 40, 1139.

[11] N. Fleck, J. Mech. Phys. Solids **1995**, 43, 1409.

[12] N. Fleck, Acta Metall. Mater. **1995**, 43, 3177.

[13] A. Akisanya, A. Cocks, N. Fleck, Int. J. Mech. Sci. **1997**, 39, 1315.

[14] N. Ogbonna, N. Fleck, Acta Metall. Mater. **1995**, 43, 603.

[15] H. Kuhn, Int. J. Powder Metall. **1971**, 7, 15.

[16] S. Shima, M. Oyane, Int. J. Mech. Sci. **1976**, 18, 285.

[17] C. Gu, M. Kim, L. Anand, Int. J. Plast. **2001**, 17, 147.

[18] T. Watson, J. Wert, Metall. Trans. A **1993**, 24, 2071.

[19] C. Tsigginos, J. Strong, A. Zavaliangos, Int. J. Solids Struct. **2015**, 60, 17.

[20] B. Harthong, J.-F. Jerier, V. Richefeu, B. Chareyre, P. Dorémus, D. Imbault, F.-V. Donzé, Int. J. Mech. Sci. **2012**, 61, 32.

[21] B. Harthong, D. Imbault, P. Dorémus, J. Mech. Phys. Solids **2012**, 60, 784.

[22] G. Petekidis, A. Moussaid, P. Pusey, Phys. Rev. E **2002**, 66, 051402.

[23] M. Haw, W. Poon, P. Pusey, Phys. Rev. E **1998**, 57, 6859.

[24] M. Toiya, J. Stambaugh, W. Losert, Phys. Rev. Lett. **2004**, 93, 088001.

[25] J. Christoffersen, M. M. Mehrabadi, S. Nemat-Nasser, J. Appl. Mech **1981**, 48, 339.

[26] H. F. Fischmeister, E. Arzt, Powder Metall. **1983**, 26, 82.

[27] S. Nemat-Nasser, J. Mech. Phys. Solids **2000**, 48, 1541.

[28] K. A. Darling, E. L. Huskins, B. E. Schuster, Q. Wei, L. J. Kecskes, Mater. Sci. Eng., A **2015**, 638, 322.

[29] K. A. Darling, M. Rajagopalan, M. Komarasamy, M. A. Bhatia, B. C. Hornbuckle, R. S. Mishra, K. N. Solanki, Nature **2016**, 537, 378.

[30] K. A. Darling, A. J. Roberts, Y. Mishin, S. N. Mathaudhu, L. J. Kecskes, J. Alloys Compd. **2013**, 573, 142.

[31] A. Bahrami, C. F. O. Carrasco, A. D. Cardona, T. Huminiuc, T. Polcar, S. E. Rodil, Surf. Coat. Technol. **2019**, 364, 22.

[32] Z. C. Cordero, B. E. Knight, C. A. Schuh, Int. Mater. Rev. **2016**, 61, 495.

[33] B. K. VanLeeuwen, K. A. Darling, C. C. Koch, R. O. Scattergood, B. G. Butler, Acta Mater. **2010**, 58, 4292.

[34] B. K. VanLeeuwen, K. A. Darling, C. C. Koch, R. O. Scattergood, Mater. Sci. Eng., A **2011**, 528, 2192.

[35] R. Takahashi, S. Takenaka, S. Sato, T. Sodesawa, K. Ogura, K. Nakanishi, J. Chem. Soc., Faraday Trans. **1998**, 94, 3161.

[36] A. A. Ward, M. R. French, D. N. Leonard, Z. C. Cordero, J. Mater. Process. Technol. **2018**, 254, 373.

[37] H. Hu, B. B. Rath, Metall. Mater. Trans. B **1970**, 1, 3181.

[38] L. Lu, N. Tao, L. Wang, B. Ding, K. Lu, J. Appl. Phys. **2001**, 89, 6408.

[39] D. Farkas, A. Frøseth, H. Van Swygenhoven, Scr. Mater. **2006**, 55, 695.

[40] G. Fan, Y. Wang, L. Fu, H. Choo, P. Liaw, Y. Ren, N. Browning, Appl. Phys. Lett. **2006**, 88, 171914.

[41] G. Fan, L. Fu, H. Choo, P. Liaw, N. Browning, Acta Mater. **2006**, 54, 4781.

[42] C. Brandl, T. C. Germann, A. G. Perez-Bergquist, E. K. Cerreta, Mater. Res. Let. **2013**, 1, 220.

[43] M. A. Atwater, K. A. Darling, M. A. Tschopp, Adv. Eng. Mater. **2016**, 18, 83.

[44] Y. Qi, A. Kosinova, A. R. Kilmametov, B. B. Straumal, E. Rabkin, Scr. Mater. **2020**, 178, 29.

[45] E. de Vries, The Ohio State University, **2004**.

[46] A. S. Khan, H. Zhang, L. Takacs, Int. J. Plast. **2000**, 16, 1459.

[47] A. S. Khan, H. Zhang, Int. J. Plast. **2000**, 16, 1477.

[48] A. S. Khan, Y. S. Suh, R. Kazmi, Int. J. Plast. **2004**, 20, 2233.

[49] R. Valiev, Y. Estrin, Z. Horita, T. Langdon, M. Zehetbauer, Y. Zhu, Mater. Res. Let. **2016**, 4, 1.

[50] C. Huang, W. Hu, Q. Wang, C. Wang, G. Yang, Y. Zhu, Mater. Res. Let. **2015**, 3, 88.

[51] M. Baig, A. S. Khan, S.-H. Choi, A. Jeong, Int. J. Plast. **2013**, 40, 65.

[52] S. A. Turnage, M. Rajagopalan, K. A. Darling, P. Garg, C. Kale, B. G. Bazehhour, I. Adlakha, B. C. Hornbuckle, C. L. Williams, P. Peralta, Nat. Comm. **2018**, 9, 1.

[53] X. An, Z. Xing, C. Jia, Metall. Mater. Trans A **2014**, 45, 2171.

[54] S. Edwards, D. Grinev, Phys. Rev. E. **1998**, 58, 4758.

[55] M. Nicolas, P. Duru, O. Pouliquen, Euro. Phys. J. E **2000**, 3, 309.

[56] P. Das, H. Vinutha, S. Sastry, Proc. Nat. Acad. Sci. **2020**, 117, 10203.

[57] Y. Wu, X. An, A. Yu, Powder Technol. **2017**, 314, 89.

[58] B. Zhao, X. An, Y. Wang, Q. Qian, X. Yang, X. Sun, Powder Technol. **2017**, 317, 171.

[59] J. Valverde, M. Quintanilla, A. Castellanos, Phys. Rev. Lett. **2004**, 92, 258303.

[60] W. Chang, I. Etsion, D. B. Bogy, J. Tribol. **1987**, 109, 257.

[61] L. Perez-Gandarillas, A. Mazor, O. Lecoq, A. Michrafy, Powder Technol. **2018**, 337, 43.

[62] A. J. Liu, S. R. Nagel, Annu. Rev. Condens. Matter Phys. **2010**, 1, 347.

[63] D. Bi, J. Zhang, B. Chakraborty, R. P. Behringer, Nature **2011**, 480, 355.

[64] D. Ishima, H. Hayakawa, Phys. Rev. E **2020**, 101, 042902.

[65] H. Brouwers, Phys. Rev. E **2014**, 89, 052211.

[66] M.-H. Hwang, H.-S. Lee, J.-H. Han, D.-H. Kim, H.-R. Cha, Mater. **2019**, 12, 824.

[67] A. A. Ward, Y. Zhang, Z. C. Cordero, Acta Mater. **2018**, 158, 393.

[68] Z. Liu, Y. Ge, D. Zhao, Y. Lou, Y. Liu, Y. Wu, P. Yu, C. Yu, Metals **2020**, 10, 971.

[69] B. Bhushan, *Modern tribology handbook*, CRC Press, Boca Raton, Fl, USA **2000**.

[70] J. Greenwood, Wear **1991**, 150, 153.

[71] N. Beeler, T. Tullis, D. Goldsby, J. Geophys. Res.: Solid Earth **2008**, 113.

[72] J. R. Rice, J. Geophys. Res.: Solid Earth **2006**, 111.

[73] *ASM Handbook: Nonferrous alloys and special-purpose materials, Vol. 2*, ASM International, OH, USA **1990**.

[74] Y. Liu, S. Zhang, Z. Han, Y. Zhao, J. Nanopart. Res. **2016**, 18, 296.

[75] K. A. Darling, S. Mathaudhu, L. Kecskes, Army Research Lab Aberdeen Proving Ground, MD, **2012**.

[76] F. Da Cruz, S. Emam, M. Prochnow, J.-N. Roux, F. Chevoir, Phys. Rev. E **2005**, 72, 021309.

[77] E. Azéma, F. Radjai, Phys. Rev. Lett. **2014**, 112, 078001.

[78] N. Berger, E. Azéma, J.-F. Douce, F. Radjai, Europhys. Let. **2016**, 112, 64004.

[79] A. Helle, K. E. Easterling, M. Ashby, Acta Metall. **1985**, 33, 2163.

[80] T. Liu, Wear **1964**, 7, 163.

[81] E. I. Corwin, H. M. Jaeger, S. R. Nagel, Nature **2005**, 435, 1075.

[82] E. I. Corwin, E. T. Hoke, H. M. Jaeger, S. R. Nagel, Phys. Rev. E **2008**, 77, 061308.

[83] T. S. Majmudar, R. P. Behringer, Nature **2005**, 435, 1079.

[84] F. Radjai, M. Jean, J.-J. Moreau, S. Roux, Phys. Rev. Lett. **1996**, 77, 274.

[85] F. Radjai, S. Roux, J. J. Moreau, Chaos: Inter. J. Nonlin. Sci. **1999**, 9, 544.

[86] S. J. Antony, Phys. Rev. E **2000**, 63, 011302.

[87] F. Bowden, D. Tabor, Proc. R. Soc. London, A **1939**, 169, 391.

[88] G. S. Kelly, S. G. Advani, J. W. Gillespie, T. A. Bogetti, J. Mater. Process. Technol. **2013**, 213, 1835.

[89] A. Siddiq, E. Ghassemieh, Mech. Mater. **2008**, 40, 982.

[90] A. Siddiq, T. El Sayed, Mater. Lett. **2011**, 65, 356.

[91] Z. Yao, G.-Y. Kim, Z. Wang, L. Faidley, Q. Zou, D. Mei, Z. Chen, Int. J. Plast. **2012**, 39, 75.

[92] V. Fartashvand, A. Abdullah, S. S. Vanini, Ultrason. Sonochem. **2017**, 38, 744.

[93] B. Langenecker, IEEE Trans. Sonics Ultrasonics **1966**, 13, 1.

[94] Y. Daud, M. Lucas, Z. Huang, J. Mater. Process. Technol. **2007**, 186, 179.

[95] A. Eaves, A. Smith, W. Waterhouse, D. Sansome, Ultrasonics **1975**, 13, 162.

[96] I. A. Gindin, G. N. Malik, I. M. Neklyudov, O. T. Rozumnyi, Sov. Phys. J. **1972**, 15, 192.

[97] H. Huang, A. Pequegnat, B. Chang, M. Mayer, D. Du, Y. Zhou, J. Appl. Phys. **2009**, 106, 113514.

[98] X. Liu, C. Wu, G. K. Padhy, Scr. Mater. **2015**, 102, 95.

[99] J.-C. Hung, C.-C. Lin, Mater. Des. **2013**, 45, 412.

[100] H. Kirchner, W. Kromp, F. Prinz, P. Trimmel, Mater. Sci. Eng. **1985**, 68, 197.

[101] R. Dutta, R. Petrov, R. Delhez, M. Hermans, I. Richardson, A. Böttger, Acta Mater. **2013**, 61, 1592.

[102] B. Cheng, H. Leung, A. Ngan, Philos. Mag. **2015**, 95, 1845.

[103] B. Langenecker, Phys. Rev. **1966**, 145, 487.

[104] K. Siu, A. Ngan, I. Jones, Int. J. Plast. **2011**, 27, 788.

[105] K. Siu, H. Liu, A. Ngan, Materialia **2019**, 5, 100214.

[106] K. Siu, A. Ngan, Mater. Sci. Eng., A **2013**, 572, 56.

[107] K. Siu, A. Ngan, Philos. Mag. **2011**, 91, 4367.

[108] B. Schinke, T. Malmberg, Nucl. Eng. Des. **1987**, 100, 281.

[109] M. Bhatia, M. Rajagopalan, K. Darling, M. Tschopp, K. Solanki, Mater. Res. Let. **2017**, 5, 48.

[110] M. Mehrabadi, S. Cowin, J. Mech. Phys. Solids **1978**, 26, 269.

[111] L. Anand, J. Mech. Phys. Solids **1983**, 31, 105.

[112] J. W. Rudnicki, J. Rice, J. Mech. Phys. Solids **1975**, 23, 371.

[113] A. A. Ward, Z. C. Cordero, Scr. Mater. **2020**, 177, 101.

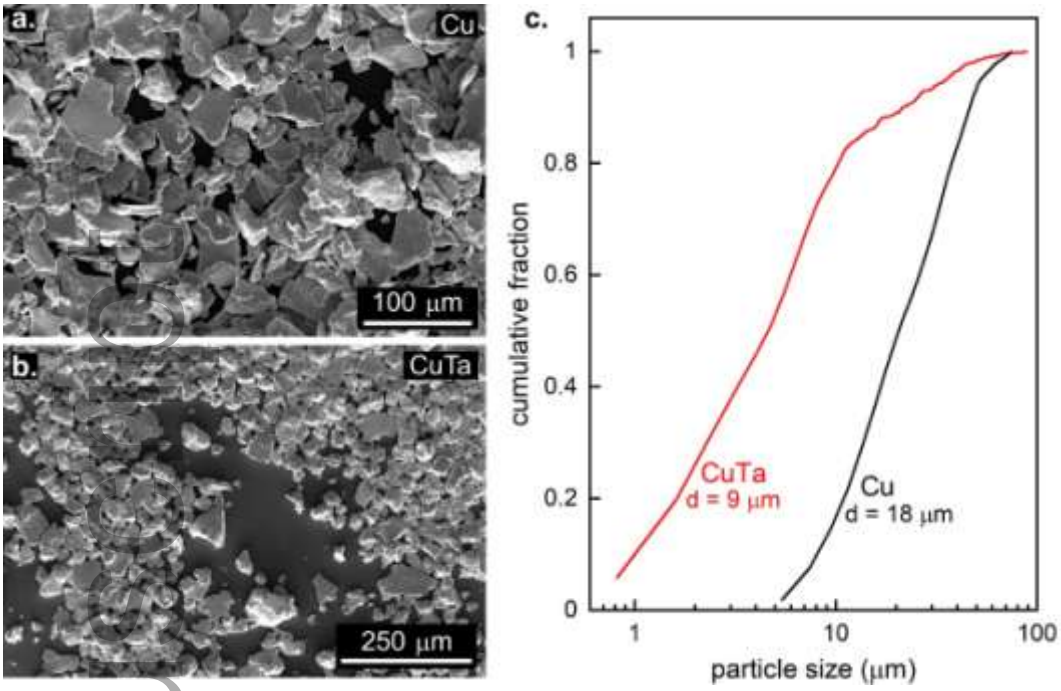

Figure 1: SEM micrographs of (a) the Cu powder and (b) the CuTa powder. (c) Cumulative particle size distributions of the feedstock powders.

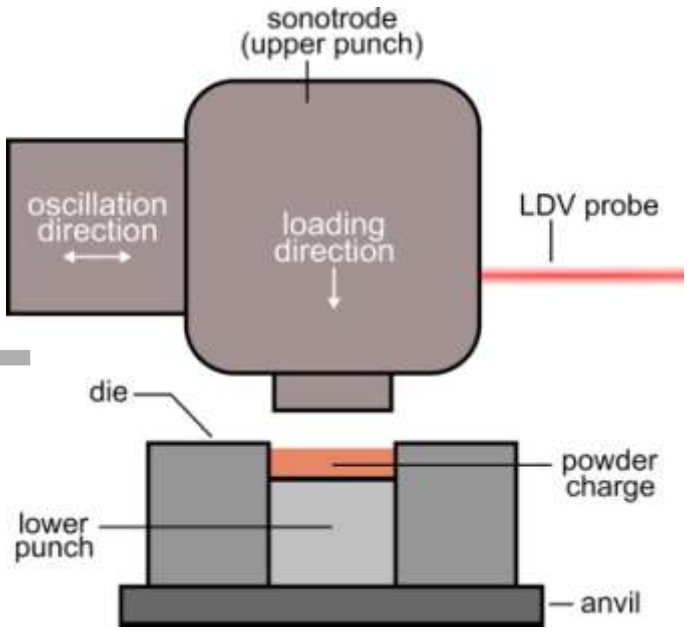

Figure 2: Instrumented ultrasonic compaction setup.

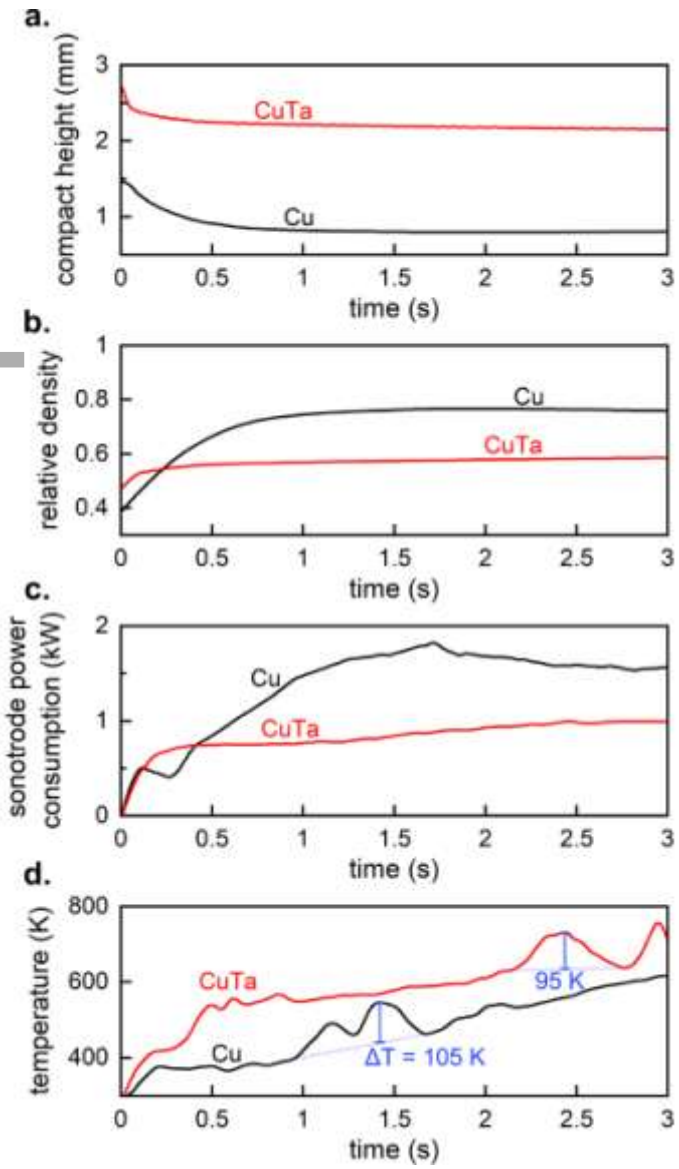

Figure 3: *In situ* measurements of (a) compact height, (b) compact relative density, (c) sonotrode power consumption, and (d) temperature during densification of nanocrystalline Cu and CuTa powders. Temperature spikes of ~100 K are labeled in (d).

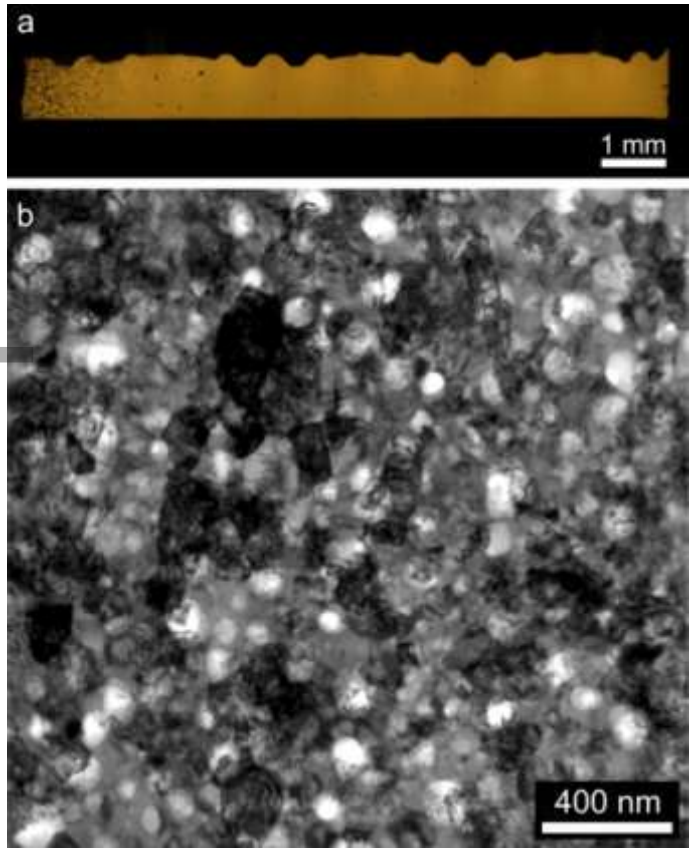

Figure 4. (a) Optical micrograph of a cross-sectioned Cu compact, densified using σ = 40 MPa, λ = 18 μm, and t_c = 2.2 seconds. (b) Bright-field TEM micrograph of a sample extracted from the center of the same compact showing nanoporosity and nanoscale grain structure.

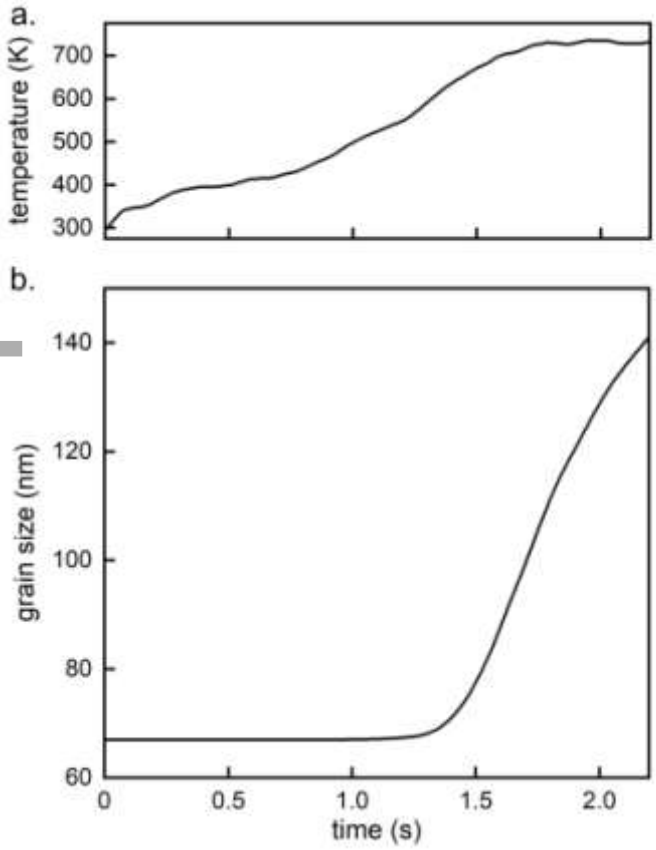

Figure 5. (a) *In situ* temperature measurements and (b) predicted grain size as a function of time during a compaction experiment performed with the same parameters as in **Figure 4**.

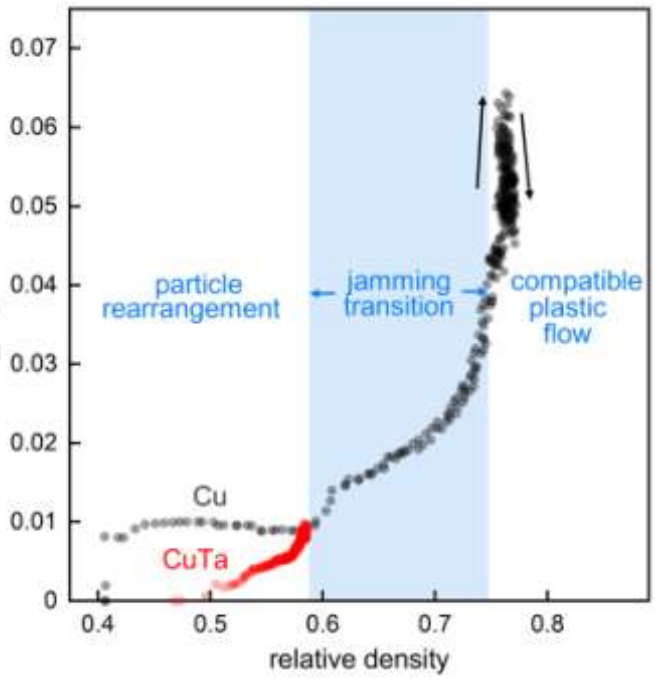

Figure 6. Geometric hardening parameter (**η**) vs. relative density for the Cu powder and the CuTa. Each dataset corresponds to a 3 second compaction cycle, and the time interval between each datapoint is 0.01 seconds.

Nomenclature

α	thermal diffusivity (m^2/s)
β	ratio of normal stress to yield strength (–)
$\dot{\gamma}$	shear strain rate (s^{-1})
D	grain size (m)
d	mean particle diameter (m)
F	packing fraction (–)
φ	standard deviation of log-normal distribution (–)
h	compact height (m)
H	hardness (GPa)
η	geometric hardening parameter (–)
I	inertial number (–)
l	mean particle contact size (m)
λ	oscillation amplitude (m)
M_0	grain boundary mobility prefactor ($m^4 \cdot K$)
m	particle mass (kg)
μ	friction coefficient (–)
n	grain growth exponent (–)
f	oscillation frequency (s^{-1})
P	sonotrode power consumption (P)
Q	activation energy for grain growth (eV)
r	radius of die (m)
$\tilde{\rho}$	relative density (–)
ρC_p	volumetric heat capacity ($J/m^3 \cdot K$)
σ	compaction normal pressure (MPa)
$\bar{\sigma}_c$	mean normal interparticle contact stress (MPa)
T	temperature (K)
T_b	bulk temperature (K)
T_f	flash heating temperature (K)
T_m	melting temperature (K)
T_0	reference temperature (K)
t	time (s)
t_c	compaction time (s)
τ_c	shear strength of particle contact (MPa)
τ_{ys}	shear strength of base material (MPa)
V	particle relative tangential velocity (m/s)

Table of Contents:

*Austin A. Ward, Christopher A. Hareland, Nathan E. Palmerio, Zachary C. Cordero**

Title: Thermally activated jamming in ultrasonic powder compaction

This work examines the role of thermal softening in ultrasonic powder compaction. Ultrasonic compaction experiments on pure Cu reveal three stages of densification characterized, respectively, by particle rearrangement, jamming, and compatible plastic deformation. Comparing the compaction behaviors of pure Cu and a thermally stable CuTa alloy demonstrates that a thermally activated jamming transition drives interparticle junction growth and densification.